ChemComm

On the Role of Wall Thickness in Determining the Plasmonic Properties of Silver-Gold Nanocages

Journal:	*ChemComm*
Manuscript ID	CC-COM-04-2023-002068.R1
Article Type:	Communication

COMMUNICATION

On the Role of Wall Thickness in Determining the Plasmonic Properties of Silver-Gold Nanocages†

Shikuan Shao, Ankai Wang, Ria Gupta, Shengli Zou* and Xiaohu Xia*

Received 00th January 20xx,
Accepted 00th January 20xx

DOI: 10.1039/x0xx00000x

This work examines the roles played by wall thickness in determining the plasmonic properties of gold-silver (Ag-Au) nanocages. Ag-Au cages with different wall thicknesses, but the same void or outer size, shape, and elemental composition, were designed as a model platform. The experimental findings were understood with theoretical calculations. This study not only investigates the effect of wall thickness but also provides an effective knob to tailor the plasmonic properties of hollow nanostructures.

Over the past several decades, plasmonic metal nanostructures have attracted significant attention as they enable localization and manipulation of light, making them a desirable choice for a variety of emerging applications such as sensing, imaging, catalysis, surface-enhanced spectroscopies, and photothermal therapies.[1-3] Among them, hollow nanostructures are known to be a preeminent class of plasmonic materials. They possess superior plasmonic properties compared to their solid counterparts owing to a phenomenon called plasmonic hybridization.[4,5] The design and development of hollow nanostructures with desired plasmonic properties oftentimes rely on careful tailoring of their physicochemical parameters, including morphologies and elemental compositions.[6,7] Among various parameters, wall thickness has been demonstrated to be a key factor in determining the plasmonic properties of hollow nanostructures. For instance, the localized surface plasmon resonance (LSPR) peak of Ag-Au nanoboxes was red-shifted when their wall thickness was reduced through chemical etching.[8] The major LSPR peaks of Au-based nanocages with thicker walls were located at shorter wavelengths.[9,10] Despite of the observations in case studies, to the best of our knowledge, systematic investigation on the impact of wall thickness on plasmonic properties of hollow nanostructures has not been reported so far. The challenge in this subject might be ascribed to the difficulty in synthesizing hollow nanostructures with different wall thicknesses, but the same sizes, shapes, and compositions.

In this work, using Ag-Au alloyed nanocages as a model system, we systematically investigate the roles played by wall thickness in determining the plasmonic properties of hollow nanostructures. The reasons why we chose to focus on Ag-Au nanocages as model hollow nanostructures are: i) They have been extensively studied and widely used in many applications, especially biomedicine;[11,12] and ii) With our recent approach based on template regeneration and galvanic replacement,[13,14] the wall thickness of Ag-Au nanocages can be finely controlled in experiments. To understand the observed wall thickness-dependent plasmonic properties, we performed theoretical simulations by employing the size-corrected discrete dipole approximation (DDA) method.

To single out the role of wall thickness, we designed two complementary sets of experiments. In the first set of experiments, we fixed the interior void size of nanocages and alternated the wall thickness by depositing Ag-Au on the outer surface of cages (see Figure 1a). These cages are termed "[Ag-Au]$_{O\text{-}n}$ nanocages" (O: wall thickness change toward outer surfaces; n: number of consecutive Ag-Au layers, n = 1, 2, 3, 4, and 5) in the following discussion. In the second set of experiments, we fixed the outer diameter of the cages and changed the wall thickness by depositing Ag-Au on the inner surfaces (Figure 2a). These cages are termed "[Ag-Au]$_{I\text{-}n}$ nanocages" (I: wall thickness change toward inner surfaces; n: number of consecutive Ag-Au layers, n = 1, 2, 3, 4, and 5). It should be mentioned that the nanocages were designed to have a well-defined cubic shape with truncations at corners, of which wall thicknesses (t) can be easily visualized and measured through electron microscopy imaging. The outer size (L, defined as the distance between two opposite outer side faces, see Figure S1) of the cages was controlled in the range of ~40-80

Department of Chemistry, University of Central Florida, Orlando, Florida 32816, United States. E-mail: Shengli.Zou@ucf.edu, Xiaohu.Xia@ucf.edu

†Electronic Supplementary Information (ESI) available: Materials, methods, and additional experimental results. See DOI: 10.1039/x0xx00000x

nm, which is attributed to their prominent LSPR peaks in the visible and near-infrared regions.[15,16]

We started with the synthesis of abovementioned nanocages. The $[Ag\text{-}Au]_{O\text{-}n}$ nanocages (n = 1-5) were synthesized by using 42.9 nm Ag cubes (Figure S2a) as sacrificial templates for galvanic replacement with Au^{3+} ions. Specifically, the $[Ag\text{-}Au]_{O\text{-}1}$ cages (Figure 1b) were synthesized through conventional galvanic replacement between these Ag cubes and Au^{3+}.[17] The $[Ag\text{-}Au]_{O\text{-}n}$ cages (n = 2-5) were prepared according to our previously reported strategy based on sequential template regeneration and galvanic replacement (Figure S1).[13] Briefly, to prepare for the $[Ag\text{-}Au]_{O\text{-}2}$ cages, the voids of $[Ag\text{-}Au]_{O\text{-}1}$ cages were refilled with Ag through size-selective growth (*i.e.*, template regeneration). The resultant $Ag@[Ag\text{-}Au]_{O\text{-}1}$ core@shell cubes were then served as new templates for continuous galvanic reaction with Au^{3+} to produce $[Ag\text{-}Au]_{O\text{-}2}$ cages (Figure 1c). By repeating such processes of sequential template regeneration and galvanic replacement, $[Ag\text{-}Au]_{O\text{-}n}$ cages (n = 3, 4, and 5, see Figure 1d-f) were obtained. Detailed synthetic procedures are provided in the Electronic Supplementary Information (ESI). As shown by the TEM images in Figure 2, the $[Ag\text{-}Au]_{O\text{-}n}$ cages have different wall thicknesses, but similar voids. By randomly analyzing 200 particles per sample, the average outer sizes (L) of the $[Ag\text{-}Au]_{O\text{-}n}$ cages (n = 1-5) were measured to be 47.5, 54.7, 61.1, 66.7, and 72.5 nm, respectively. Their average wall thicknesses (t) were measured to be 4.6, 8.2, 11.4, 14.2, and 17.1 nm, respectively. These measurements indicated that the size of void (L', defined as the distance between two opposite inner side faces, see Figure S1) of the $[Ag\text{-}Au]_{I\text{-}n}$ cages were similar, with an average of 38.3 nm.

The $[Ag\text{-}Au]_{I\text{-}n}$ nanocages (n = 1-5) were synthesized using Ag cubes of 5 different sizes (*i.e.*, 64.4, 60.0, 55.2, 50.3, and 42.9 nm, see Figure S2a-e) as sacrificial templates for galvanic replacement with Au^{3+}. The $[Ag\text{-}Au]_{I\text{-}1}$ cages (Figure 2b) were prepared through conventional galvanic replacement between 64.4 nm Ag cubes and Au^{3+}.[17] To prepare for the $[Ag\text{-}Au]_{I\text{-}n}$ cages (n = 2-5), Ag cubes of 60.0, 55.2, 50.3, and 42.9 nm were first reacted with Au^{3+} through conventional galvanic replacement to generate singly-walled Ag-Au cages. These cages were then subject to the abovementioned processes of sequential template regeneration and galvanic replacement (Figure S1) for 1, 2, 3, and 4 times, respectively, which resulted in the formation of $[Ag\text{-}Au]_{I\text{-}n}$ cages (n = 2-5, see Figure 2c-f). Detailed synthetic procedures are provided in the ESI. As shown by the TEM images in Figure 2, these $[Ag\text{-}Au]_{I\text{-}n}$ cages (n = 1-5) have different wall thicknesses, but similar outer sizes (L, roughly 72.5 nm). Their average wall thicknesses (t) were measured to be 5.1, 7.6, 12.6, 14.9, and 17.1 nm, respectively. As the wall thickness or value of n increased, the size of void (L') of $[Ag\text{-}Au]_{I\text{-}n}$ cages decreased from 62.3 nm to 57.3, 47.3, 42.7, and 38.3 nm, respectively.

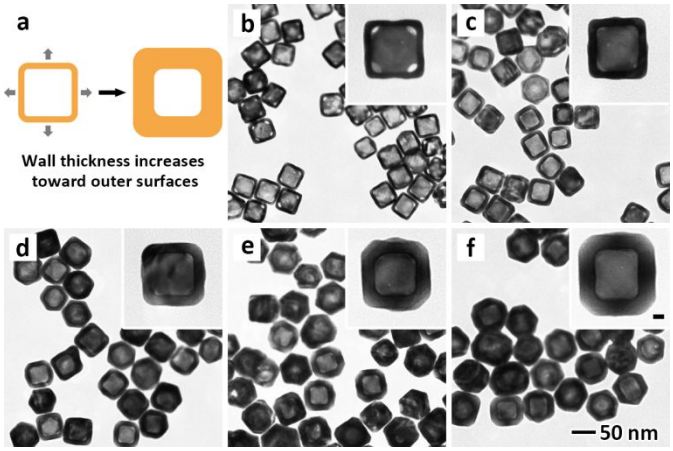

Fig. 1. $[Ag\text{-}Au]_{O\text{-}n}$ cages (O: wall thickness change toward outer surfaces; n: number of consecutive Ag-Au layers, n = 1, 2, 3, 4, and 5) that have fixed void size, but different wall thicknesses. (a) Schematics showing the process for preparing these cages. (b-f) TEM images of $[Ag\text{-}Au]_{O\text{-}1}$, $[Ag\text{-}Au]_{O\text{-}2}$, $[Ag\text{-}Au]_{O\text{-}3}$, $[Ag\text{-}Au]_{O\text{-}4}$, and $[Ag\text{-}Au]_{O\text{-}5}$ cages, respectively. Insets show individual cages at a higher magnification. The scale bar in the inset of (f) is 10 nm. The scale bars in (f) apply to all TEM images in (b-f).

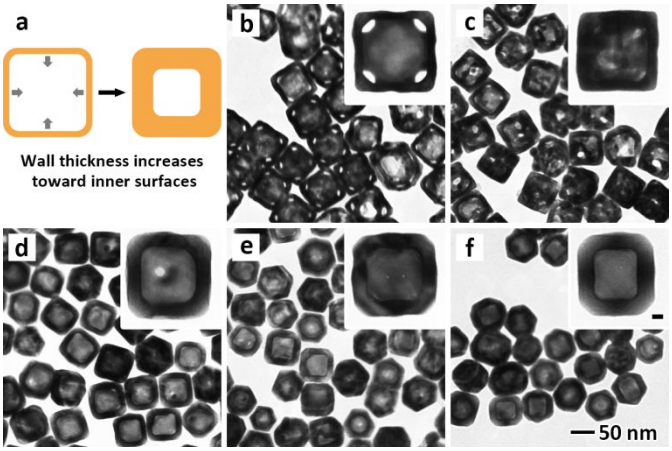

Fig. 2. $[Ag\text{-}Au]_{I\text{-}n}$ cages (I: wall thickness change toward inner surfaces; n: number of consecutive Ag-Au layers, n = 1, 2, 3, 4, and 5) that have fixed outer size, but different wall thicknesses. (a) Schematics showing the process for preparing these cages. (b-f) TEM images of $[Ag\text{-}Au]_{I\text{-}1}$, $[Ag\text{-}Au]_{I\text{-}2}$, $[Ag\text{-}Au]_{I\text{-}3}$, $[Ag\text{-}Au]_{I\text{-}4}$, and $[Ag\text{-}Au]_{I\text{-}5}$ cages, respectively. Insets show individual cages at a higher magnification. The scale bar in the inset of (f) is 10 nm. The scale bars in (f) apply to all TEM images in (b-f).

It should be pointed out that the TEM images in Figures 1 and 2 show two-dimensional projection images of cages. To resolve the three-dimensional morphologies of the cages, we performed scanning electron microscopy (SEM) imaging. As shown by the SEM images in Figures S3 and S4, all the $[Ag\text{-}Au]_{O\text{-}n}$ and $[Ag\text{-}Au]_{I\text{-}n}$ cages display a cubic shape with significant truncations at corners (*i.e.*, cuboctahedrons). Pores can be observed in the truncated corners, especially for the cages with relatively thin walls. In addition to morphologies, we also determined elemental composition of these cages. The average molar ratios of Ag to Au in all the $[Ag\text{-}Au]_{O\text{-}n}$ and $[Ag\text{-}Au]_{I\text{-}n}$ cages were measured to be roughly 1:1 by inductively coupled plasma mass spectrometry (ICP-MS) analysis (coefficient of variation < 10%).[18] The energy-dispersive X-ray (EDX) mapping images of individual cages (Figure S5) revealed that Ag and Au co-exist in the cages in the form of alloy, which is consistent with the observations in our previous studies.[13,19] Taken together, these two sets of Ag-Au cages, which have the same void or outer size, shape, and elemental composition, but different wall thicknesses, could serve as an ideal platform to investigate the role of wall thickness in determining the plasmonic properties.

We then evaluated the plasmonic properties of as-prepared

Ag-Au cages by analyzing their extinction spectra using a UV-vis spectrophotometer. Figure 3a and 3b show normalized UV-vis spectra recorded from the aqueous suspensions of the [Ag-Au]$_{O\text{-}n}$ cages (samples in Figure 1) and [Ag-Au]$_{I\text{-}n}$ cages (samples in Figure 2), respectively. A general trend observed in the spectra is that the major LSPR peaks (λ_{max}) tended to shift to shorter wavelengths (blue shift) as the wall thickness of the cages increased. More specifically, for the [Ag-Au]$_{O\text{-}n}$ cages (n = 1-5), the major LSPR peak blue-shifted continuously from 738 nm to 625, 582, 563, and 555 nm as the wall thickness increased from 4.6 nm to 8.2, 11.4, 14.2, and 17.1 nm, respectively (Figure 3a). Meanwhile, the bandwidth of the LSPR peaks slightly decreased as the wall thickness increased. With respect to the [Ag-Au]$_{I\text{-}n}$ cages (n = 1-5), their major LSPR peaks shifted from 796 nm to 688, 590, 570, and 555 nm as the wall thickness increased from 5.1 nm to 7.6, 12.6, 14.9, and 17.1 nm, respectively. Interestingly, the decrease in the bandwidths of these peaks was much more evident compared to the [Ag-Au]$_{O\text{-}n}$ cages. This observation indicates that the bandwidth of LSPR peaks of Ag-Au cages is determined by both wall thickness and void size.

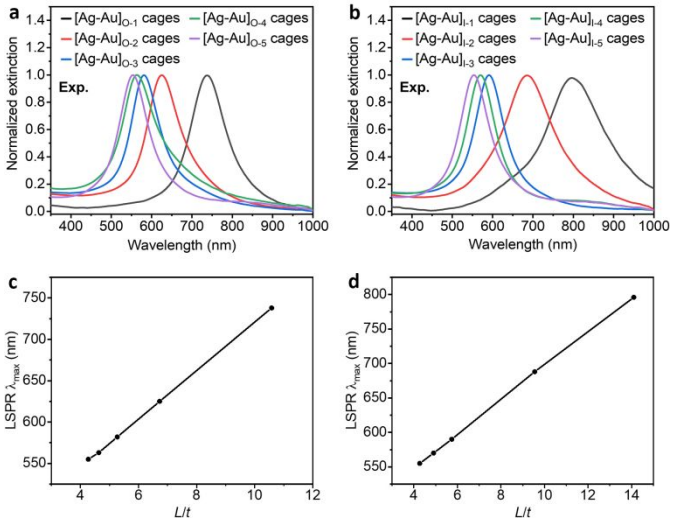

Fig. 3. Plasmonic properties of different Ag-Au cages obtained from experiments. (a, b) Normalized UV-vis spectra recorded from aqueous suspensions of different [Ag-Au]$_{O\text{-}n}$ cages (a) and [Ag-Au]$_{I\text{-}n}$ cages (b) shown in Figures 1 and 2 (as marked on the spectra). (c, d) Plots of the major LSPR peaks λ_{max} (LSPR λ_{max}) of [Ag-Au]$_{O\text{-}n}$ cages (c) and [Ag-Au]$_{I\text{-}n}$ cages (d) against the ratio of outer size to wall thickness (L/t).

As another point of interest, we found that both types of cages show linear relationships (see Figure 3c, d) between LSPR λ_{max} and their outer size to wall thickness ratio (L/t). In contrast, in the case of Au or Ag nanorods, such a linear relationship was found toward the aspect ratio of rods (*i.e.*, length divided by width).[20] Notably, the two sets of linear fittings in Figure 3c, d are not the same. The variations in slopes and intercepts might be related to the other parameters of the cages (*e.g.*, detailed morphologies and pore sizes/distributions in cage walls), which deserves careful examinations in future studies. It is worth mentioning that the variation of outer size of cages (L) is not significant in this study (in the range of ~40-80 nm). Therefore, linear relationships could also be observed by plotting the LSPR λ_{max} against the reciprocal of wall thickness ($1/t$, see Figure S6). In a sense, for Ag-Au cages of similar sizes, one can predict the trend of major LSPR peak changes on the basis of wall thickness.

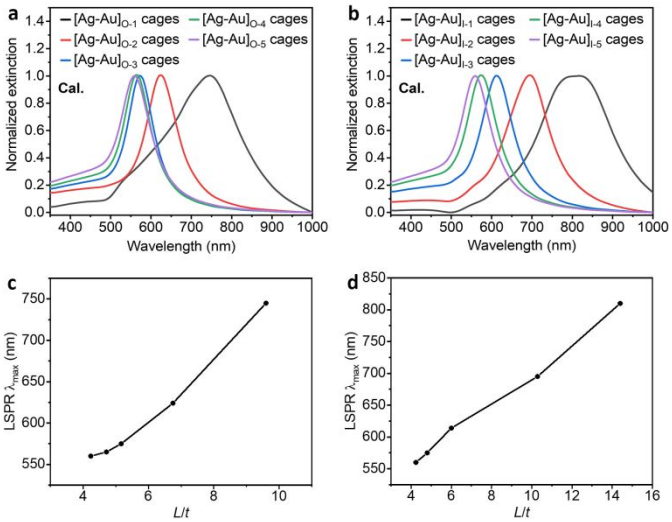

Fig. 4. Plasmonic properties of different Ag-Au cages obtained from calculations. (a, b) Normalized extinction spectra of [Ag-Au]$_{O\text{-}n}$ cages (a) and [Ag-Au]$_{I\text{-}n}$ cages (b) calculated from DDA simulation. (c, d) Plots of the calculated LSPR λ_{max} of [Ag-Au]$_{O\text{-}n}$ cages (c) and [Ag-Au]$_{I\text{-}n}$ cages (d) against the ratio of outer size to wall thickness (L/t).

To gain a deeper insight into the impact of wall thickness on plasmonic properties of Ag-Au cages, size-corrected discrete dipole approximation (DDA) simulations were performed to calculate the extinction spectra.[21,22] The theoretical models for the simulations were hollow cuboctahedron shapes with pores on each triangular side faces. Each nanocage was divided into N polarizable dipoles with a length of one nanometer in all calculations. Therefore, the physical parameters of the cages measured from TEM images were rounded to integer numbers during the simulations. Details about the cage models and physical parameters are provided in the ESI. The composition of the cage walls was treated as a homogeneous Ag-Au alloy with a molar ratio of 1:1. The calculated normalized extinction spectra of [Ag-Au]$_{O\text{-}n}$ cages and [Ag-Au]$_{I\text{-}n}$ cages are shown in Figure 4a and 4b, respectively. Overall, the observations of LSPR peaks were similar to the experimental data shown in Figure 3, where the major LSPR peaks of both types of cages gradually blue shifted with increasing wall thicknesses. Furthermore, plots of calculated LSPR λ_{max} *versus* L/t for both [Ag-Au]$_{O\text{-}n}$ and [Ag-Au]$_{I\text{-}n}$ cages (Figure 4c,d) showed good linear relationships, which is also consistent with the experimental results shown in Figure 3c,d. It should be mentioned that the exact peak positions and shapes in the calculated spectra did not agree perfectly with those in the experimental spectra. These differences could be attributed to the disparities of nanocage morphologies and compositions (*e.g.*, shape, size, wall thickness, and elemental distributions) in real samples.[23] The experimental data reflect aggregated spectra of all variations of these parameters among cages. In contrast, the simulated data display the spectra of ideal cages with perfectly uniform physiochemical parameters. Nevertheless, the simulation results and experimental results are overall in good agreement with each other.

In addition to LSPR peak positions, we have also investigated the impact of wall thickness on extinction intensities of Ag-Au cages. Herein, the particle concentration of aqueous suspensions of different cages was fixed at a constant (~6.6 x 10^{-12} M), at which the extinction intensities were in the range of ~0.2-1.0. For $[Ag\text{-}Au]_{O\text{-}n}$ cages, their aqueous suspensions displayed a distinct color change from almost colorless to cyan, navy blue, violet, and magenta (Figure S7a) as the wall thickness increased. Their experimental extinction spectra (Figure S7b) indicated that extinction intensities increased dramatically with increasing wall thickness, which is in good agreement with the calculated spectra (Figure S7c). The peak extinction of $[Ag\text{-}Au]_{O\text{-}5}$ cage was almost 5-fold greater than that of the $[Ag\text{-}Au]_{O\text{-}1}$ cage in both experimental and simulated spectra. This observation suggests that extinction intensity of Ag-Au cages with a fixed void size is positively correlated with wall thickness. For $[Ag\text{-}Au]_{I\text{-}n}$ cages, the color of their aqueous suspensions changed from light grey to cyan, blue, violet, and magenta (Figure S8a) with increasing wall thickness. Compared to aforementioned $[Ag\text{-}Au]_{O\text{-}n}$ cages, the difference in extinction intensities of these $[Ag\text{-}Au]_{I\text{-}n}$ cages were less significant, according to both experimental and calculated spectra (Figure S8b, c). The extinction intensity of $[Ag\text{-}Au]_{I\text{-}5}$ cage was about 2 times higher than that of the $[Ag\text{-}Au]_{I\text{-}1}$ and $[Ag\text{-}Au]_{I\text{-}2}$ cages, and was similar compared to the extinction intensities of $[Ag\text{-}Au]_{I\text{-}3}$ and $[Ag\text{-}Au]_{I\text{-}4}$ cages. This observation implies that the increased extinction intensity caused by the increase of wall thickness was somewhat offset by the reducing void sizes or inner surface areas. Collectively, these results demonstrate that the extinction intensity of Ag-Au nanocages is influenced by both wall thickness and void size, where wall thickness plays a dominating role.

It should be noted that size correction of the Ag and Au dielectric constants was taken into account in numerical simulations (Figures 4a, 4b, S7c, and S8c).[22] When the calculations were performed without size corrections, the theoretical and experimental results of the $[Ag\text{-}Au]_{O\text{-}n}$ cages, in terms of both LSPR peak shapes and intensities, still agree well with each other (Figures S7b, d). For the $[Ag\text{-}Au]_{I\text{-}n}$ cages, however, a doublet peak in the calculated spectrum was observed for the $[Ag\text{-}Au]_{I\text{-}1}$ cage (Figure S8d), as opposite to a single peak in the experimental spectrum (Figure S8b). Meanwhile, the calculated LSPR peak intensities for the $[Ag\text{-}Au]_{I\text{-}n}$ cages were quite different from the experimental data (Figure S8b,d). This observation illustrates the importance of considering size correction in the numerical simulations when the wall thickness of nanocages is small.

In conclusion, we have systematically investigated the role of wall thickness in determining the plasmonic properties of Ag-Au nanocages from both experimental and theoretical aspects. Two complementary types of Ag-Au nanocage samples were designed and synthesized: one is $[Ag\text{-}Au]_{O\text{-}n}$ cage (*n*: number of consecutive Ag-Au layers, *n* = 1-5) that have different wall thickness, but the same void size; another is $[Ag\text{-}Au]_{I\text{-}n}$ cages (*n* = 1-5) with different wall thickness and a fixed outer size. We found that, in both types of Ag-Au nanocages, the major LSPR peak (λ_{max}) was directly proportional to the ratio of outer size to wall thickness (L/t) with quality linear relationships. Analysis of aqueous suspensions of the Ag-Au cages at the same particle concentration indicated that wall thickness also has a direct impact on extinction intensities of the cages. We believe the findings and insights from this work will inspire both fundamental and applied research in the future.

This study was supported in part by a grant from the National Science Foundation (DMR-2004546) and the faculty startup funds from the University of Central Florida (UCF).

Conflicts of interest

The authors declare no conflict of interest.

References

1 K. M. Mayer and J. H. Hafner, *Chem. Rev.*, 2011, **111**, 3828-3857.
2 Y. Xia, W. Li, C. M. Cobley, J. Chen, X. Xia, Q. Zhang, M. Yang, E. C. Cho and P. K. Brown, *Acc. Chem. Res.*, 2011, **44**, 914-924.
3 E. Cortes, L. V. Besteiro, A. Alabastri, A. Baldi, G. Tagliabue, A. Demetriadou and P. Narang, *ACS Nano*, 2020, **14**, 16202-16219.
4 E. Prodan, C. Radloff, N. J. Halas and P. Nordlander, *Science*, 2003, **302**, 419-422.
5 E. Prodan and P. Nordlander, *J. Chem. Phys.*, 2004, **120**, 5444-5454.
6 X. Xia, Y. Wang, A. Ruditskiy and Y. Xia, *Adv. Mater.*, 2013, **25**, 6313-6333.
7 X. Wang, J. Feng, Y. Bai, Q. Zhang and Y. Yin, *Chem. Rev.*, 2016, **116**, 10983-11060.
8 X. Lu, L. Au, J. McLellan, Z.-Y. Li, M. Marquez and Y. Xia, *Nano Lett.*, 2007, **7**, 1764-1769.
9 L. Au, X. Lu and Y. Xia, *Adv. Mater.*, 2008, **20**, 2517-2522.
10 A. Shakiba, S. Shah, A. C. Jamison, I. Rusakova, T. C. Lee and T. R. Lee, *ACS Omega*, 2016, **1**, 456-463.
11 S. E. Skrabalak, J. Chen, L. Au, X. Lu, X. Li and Y. Xia, *Adv. Mater.*, 2007, **19**, 3177-3184.
12 Z. Qin, Y. Zheng, T. Du, Y. Wang, H. Gao, X. Wang and H. Jiang, *J. Chem. Eng.*, 2022, **450**, 138322.
13 Z. Gao, H. Ye, Q. Wang, M. J. Kim, D. Tang, Z. Xi, Z. Wei, S. Shao and X. Xia, *ACS Nano*, 2020, **14**, 791-801.
14 Z. Gao, S. Shao, W. Gao, D. Tang, D. Tang, S. Zou, M. J. Kim and X. Xia, *ACS Nano*, 2021, **15**, 2428-2438.
15 C. Wang, Y. Wang, L. Zhang, R. J. Miron, J. Liang, M. Shi, W. Mo, S. Zheng, Y. Zhao and Y. Zhang, *Adv. Mater.*, 2018, **30**, e1804023.
16 L. Zhang, J. Pan, Y. Long, J. Li, W. Li, S. Song, Z. Shi and H. Zhang, *Small*, 2019, **15**, e1903182.
17 S. E. Skrabalak, L. Au, X. Li and Y. Xia, *Nat. Protoc.*, 2007, **2**, 2182-2190.
18 Z. Xi, K. Wei, Q. Wang, M. J. Kim, S. Sun, V. Fung and X. Xia, *J. Am. Chem. Soc.*, 2021, **143**, 2660-2664.
19 S. Shao, X. Zhu, V. Ten, M. J. Kim and X. Xia, *J. Phys. Chem. C*, 2022, **126**, 7337-7345.
20 S. Link and M. A. El-Sayed, *J. Phys. Chem. B*, 1999, **103**, 8410.
21 B. T. Draine and P. J. Flatau, *J. Opt. Soc. Am. A*, 1994, **11**, 1491-1499.
22 E. A. Coronado and G. C. Schatz, *J. Chem. Phys.*, 2003, **119**, 3926-3934.
23 M. Hu, H. Petrova, A. R. Sekkinen, J. Chen, J. M. McLellan, Z.-Y. Li, M. Marquez, X. Li, Y. Xia and G. V. Hartland, *J. Phys. Chem. B*, 2006, **110**, 19923-19928.